Dew-Point Measurements for Water in Compressed Carbon Dioxide

Christopher W. Meyer
Sensor Science Div., National Institute of Standards and Technology, Gaithersburg, MD 20899

Allan H. Harvey
Applied Chemicals and Materials Div., National Institute of Standards and Technology, Boulder, CO 80305

DOI 10.1002/aic.14818
Published online August 7, 2015 in Wiley Online Library (wileyonlinelibrary.com)

When transporting CO_2 for sequestration, it is important to know the water dew point in order to avoid condensation that can lead to corrosion. A flow apparatus to measure the water content at saturation in a compressed gas has been constructed. A saturator humidifies the flowing gas by equilibrating it with liquid water. Then, a gravimetric hygrometer measures the water mole fraction of the humid gas. Dew-point data for H_2O in CO_2 on six isotherms between 10 and 80 °C at pressures from 0.5 to 5 MPa are reported. The uncertainties in water content at the dew point (expanded uncertainty with coverage factor $k = 2$) are on average 0.3%, significantly smaller than in any previous work. The data have been analyzed to extract the interaction second virial coefficient; the values are consistent with the theoretical estimates of Wheatley and Harvey but have a much smaller uncertainty. Published 2015 American Institute of Chemical Engineers *AIChE J*, 61: 2913–2925, 2015
Keywords: thermodynamics/classical, phase equilibrium, carbon dioxide, dew point, phase equilibrium, virial coefficients, water

Introduction

Knowledge of the thermophysical properties of mixtures containing CO_2 and H_2O is important for many applications. One such property of current interest is the water dew-point temperature in CO_2, which is dependent on the moisture content and pressure of the gas. Knowledge of this property is needed for CO_2 transportation in pipelines for carbon capture and sequestration,[1] because CO_2 captured from power plants contains moisture. Before this CO_2 is transported, its moisture content must be reduced to the point where it will not condense and cause corrosion. The relation between the dew-point temperature, water content, and pressure is important for determining the degree to which the CO_2 must be dried before transportation. Better understanding of thermodynamics of mixtures containing CO_2 and H_2O is also important for the design and optimization of advanced power cycles that facilitate carbon capture.[2,3]

The dew-point temperature is defined as the temperature at which liquid water and water in the vapor phase are in equilibrium. T_{DP} is related to the water-vapor amount (mole) fraction y_w and gas pressure p by iteratively solving the equation

$$y_w = \frac{e(T)}{p} f(T,p) \tag{1}$$

where T is the absolute temperature and it is understood that $T = T_{DP}$. Here, $e(T)$ is the saturated water vapor pressure at T.[4] The water vapor enhancement factor $f(T, p)$ reflects departures from ideal solution behavior and nonideal gas effects[5] and is a gas-dependent property. Unfortunately, for CO_2-H_2O mixtures there is limited theoretical information and only scattered experimental data on $f(T, p)$ at the temperatures relevant for pipeline transport.

Existing experimental data for the water vapor enhancement factor $f(T, p)$ in compressed CO_2 at moderate pressures (below about 10 MPa) were reviewed in 2011 by Wheatley and Harvey.[6] Especially at relatively low temperatures relevant to pipeline transport, the existing experimental data[7–11] were found to be mutually inconsistent. A recent experimental study[12] also covered the region of interest, but the dew-point measurements at low temperatures had large uncertainties.

The value of $f(T, p)$ can be calculated[5] using relevant virial coefficients found in a series expansion for the deviation of a fluid from ideal-gas behavior

$$\frac{p}{\rho RT} = 1 + B\rho + C\rho^2 + \ldots \tag{2}$$

where p is the pressure, ρ is the molar density, and R is the molar gas constant. B and C are the second and third virial coefficients, respectively. For pressures up to a few MPa, it is sufficient for many purposes to truncate Eq. 2 after the C term, or even after the B term at sufficiently low pressure.

For a binary mixture, B and C are rigorously given as a function of amount fractions y_1 and y_2 by

$$B_{mix} = y_1^2 B_{11} + 2y_1 y_2 B_{12} + y_2^2 B_{22} \tag{3}$$

$$C_{mix} = y_1^3 C_{111} + 3y_1^2 y_2 C_{112} + 3y_1 y_2^2 C_{122} + y_2^3 C_{222} \tag{4}$$

For CO_2-H_2O mixtures, the virial coefficients B_{11} and B_{22} correspond to the second virial coefficients of pure CO_2 and

Correspondence concerning this article should be addressed to A. H. Harvey at allan.harvey@nist.gov.

pure H_2O, respectively, and C_{111} and C_{222} correspond to the third virial coefficients of pure CO_2 and pure H_2O, respectively. The values of these coefficients are well known.[13–15] Recently, Wheatley and Harvey[6] calculated the interaction second virial coefficient B_{12}, which describes the interaction between one H_2O molecule and one CO_2 molecule. B_{12} was derived as a function of temperature using a potential-energy surface obtained from high-level quantum calculations. With appropriate thermodynamic manipulations, Eqs. 2–4 lead to expressions for the fugacity coefficients needed to describe equilibrium between coexisting phases, enabling calculation of $f(T, p)$. The value of $f(T, p)$ depends strongly on B_{12} at all pressures. At high pressures, $f(T, p)$ also depends on C_{112} and (to a much lesser extent) C_{122}.

Because of limitations on the accuracy of quantum calculations in reasonable computer time, the potential-energy surface of Wheatley and Harvey[6] had a significant amount of uncertainty, which propagates into uncertainty in B_{12}. This uncertainty becomes larger at lower temperatures, and at pipeline temperatures is large enough to lead to uncertainty in the dew-point temperature on the order of 3–5 K for pressures on the order of 5 MPa (or uncertainty on the order of 15% for the water mole fraction at a fixed temperature).

To reduce this uncertainty, we have measured dew-point compositions along several isotherms with an accuracy that greatly exceeds that of previous work. The measurements were taken over the range 10 °C $\leq t \leq$ 80 °C (t is the Celsius temperature) and 0.5 MPa $\leq p \leq$ 5 MPa. The resulting data provide a test of the accuracy of the $B_{12}(T)$ derived by Wheatley and Harvey, and allow more accurate modeling of this important system.

Experimental

Our dew-point measurements were performed in a facility that has two main components. The first component is a saturation system in which liquid water is equilibrated with the working gas at a precisely controlled temperature and pressure. The saturator temperature is the dew-point temperature corresponding to the pressure in the vessel and the water amount fraction generated. The second component is the NIST gravimetric hygrometer,[16] an apparatus that measures the water amount fraction in a gas by separating the water from the gas using desiccants and subsequently determining the amount of each independently. Using the value of y_w measured by the gravimetric hygrometer and the values of T and p measured in the saturator, f can be determined by manipulating Eq. 1 to yield

$$f(T,p) = \frac{y_w p}{e(T)} \tag{5}$$

CO_2 and H_2O sources

The CO_2 used came from a single gas cylinder. The purity of the CO_2, as given by the gas supplier, was 99.993%. Principal impurities were N_2 (<50 ppm), H_2 (<5 ppm), Ar (<5 ppm), CO (<5 ppm), and water (<5 ppm). We did not perform a separate analysis of the gas purity. A high-purity regulator was used with the CO_2 cylinder.

The water in the saturator came from a commercial distillation system. The water source for the distillation system was tap water that passed through a paper filter, a carbon filter, and a scale-removal filter. The distilled water was stored in a polypropylene container before being placed in the saturator. The water in the saturator was changed weekly.

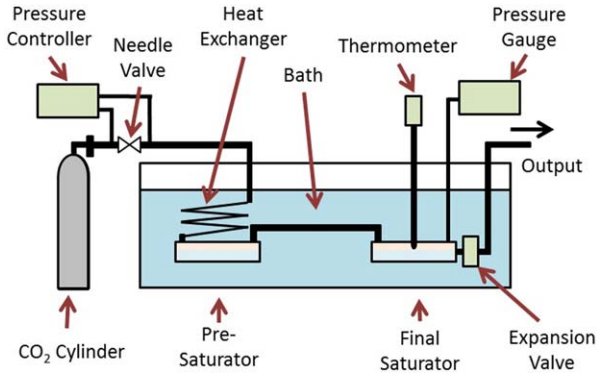

Figure 1. Saturation component for the dew-point measurement facility.

[Color figure can be viewed in the online issue, which is available at wileyonlinelibrary.com.]

Manifold and pressure control

The manifold between the gas cylinder and the inlet of the saturation system was composed of electropolished stainless-steel tubing of outer diameter 0.635 cm and wall thickness 0.09 cm. The gas flowed from the cylinder through a needle valve and then into the saturation system at the desired pressure and flow rate (typically 1–5 standard liters per minute [SLM]). The gas also flowed in parallel through a commercial pressure controller, which kept the downstream pressure constant to within 0.01%. The upper limit of the controller was 7 MPa. The needle valve was used because the pressure controller could not otherwise control the pressure for the flow rates used.

The water amount fraction generated from the saturation system usually corresponded to a dew-point temperature that was below the ambient temperature (at ambient pressure). For this case, the manifold between the outlet of the saturation system and the inlet of the gravimetric hygrometer was electropolished stainless-steel tubing of outer diameter 0.635 cm and wall thickness 0.09 cm. For the case when the dew-point temperature was above ambient temperature, commercially made heated flexible tubing was used and controlled at approximately 120 °C.

Saturation system

The saturation system, shown in Figure 1, consisted of three elements: a heat exchanger, a presaturator, and a final saturator. The gas flowed through each of these elements in the order mentioned. All elements were immersed in a commercial temperature-controlled bath of volume 95 L. They were placed in the section of the bath that was unobstructed by stirrers; this section had horizontal dimensions 69.9 cm×27.9 cm and depth 33 cm (a volume of 64 L). Based on measurements performed in a similar bath,[17] we estimate the bath temperature was stable to within 0.001 °C over the range 10 °C $\leq t \leq$ 80 °C. We estimate it was uniform to within 0.001 °C over the range 10 °C $\leq t \leq$ 40 °C and within 0.008 °C over the range 40 °C $\leq t \leq$ 80 °C. We also estimate that the temperature stability and uniformity of the saturators were those of the bath.

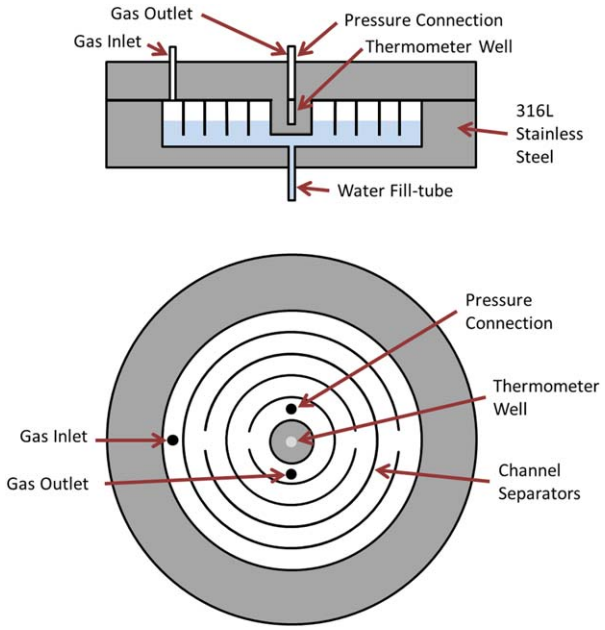

Figure 2. Schematic diagram of the saturators.

[Color figure can be viewed in the online issue, which is available at wileyonlinelibrary.com.]

The heat exchanger was designed to bring the temperature of the flowing gas to the temperature of the saturator. It was composed of a single electropolished stainless-steel tube of outer diameter 0.635 cm and wall thickness 0.09 cm. The length of the heat exchanger was 10 m. It was bent into a spiral coil of diameter 23 cm. The exchanger was attached to the presaturator using VCR* fittings.

The presaturator and final saturator had identical designs but different functions. The presaturator performed almost all of the saturation. The final saturator made small final adjustments to the saturation and was the location where the pressure and temperature measurements took place. This separation of functions is common to metrology-grade saturators. It is done because the large amount of evaporation in the presaturator causes unacceptable temperature nonuniformities. Very little water evaporates in the final saturator, so the temperature inside is very uniform.

The design of the presaturator and final saturator, shown schematically in Figure 2, was based on the "dish" design used by Hyland and Wexler.[18] Each saturator was made of two machined disks of 316L stainless steel of diameter 19.4 cm that were clamped together by 12 stainless-steel bolts of diameter 1.25 cm. The bottom disk was 3.5 cm thick and contained a cylindrical cavity of diameter 13.1 cm and depth 1.78 cm (volume 239 mL). This cavity was typically filled with 120 mL of distilled water, resulting in a fill level of about 0.9 cm. The water was filled through a tube of diameter 0.635 cm attached to the bottom of the cavity; this tube was normally sealed with a valve except when filling or emptying the saturator water. The center of the cavity bottom was 0.13 cm deeper than on the sides to ensure that all the water could drain through the fill tubes.

*Certain commercial products are identified in this article but only in order to adequately specify the procedure. Such identification neither constitutes nor implies recommendation or endorsement by either the U.S. government or the National Institute of Standards and Technology.

The gas entered each saturator from the top of the cavity through a 0.635-cm tube located at a distance of 6.0 cm from the axial center. The gas exited the saturator through a 0.635-cm tube located in the top of the cavity at a distance of 1.5 cm from the axial center. All fittings used to attach tubing to the saturator were of the VCR type. The gas flowed through a set of circularly concentric channels of 1.25 cm width as it passed through the cavity (see Figure 2). The channels were created by circular channel separators of thickness 0.13 cm and height 0.63 cm that were part of the top piece of the saturator. The gas passed from the outer channels to the inner channels through openings in the channel separators of width 1.25 cm. The cavity was bounded by the disk material on the top, sides, and bottom with thickness 2.54 cm, 3.14 cm, and 1.71 cm, respectively. The two disks were sealed together by a Viton O-ring with thickness 0.16 cm and diameter 14.3 cm. Finite-element analysis was used to determine that the saturator could withstand 11 MPa of pressure inside the cavity.

A photograph of the final saturator is shown in Figure 3. An expansion (needle) valve separated the final saturator from the manifold leading to the gravimetric hygrometer, allowing pressurization of the saturation system. The axis of the knob to the valve was vertical so that the knob could be adjusted using an attached rod protruding outside the bath. An industrial platinum resistance thermometer (PRT) was immersed in a well of diameter 0.318 cm and depth 2.22 cm located in the center of the top disk. The PRT was calibrated by comparing against a reference PRT calibrated by the NIST Thermodynamic Metrology Group. A tube leading to a commercial strain-gauge pressure transducer was attached to the top disk 1.5 cm from the axial center (this tube was sealed for the presaturator). The transducer had a range of 6.9 MPa and was calibrated by the NIST Thermodynamic Metrology Group.

Gravimetric hygrometer

This NIST gravimetric hygrometer has previously been described in detail.[16] Briefly, it separates the water from the gas in water collection tubes, using desiccants to perform the separation. Subsequently, the water mass m_w and the gas mass m_g are determined independently. The water amount fraction is then determined by

$$y_w \equiv \frac{n_w}{n_w + n_g} = \frac{m_w/M_w}{m_w/M_w + m_g/M_g} \tag{6}$$

where n_w and n_g are the amounts of water and gas in moles, respectively, and M_w and M_g are the molar masses of water and gas, respectively.

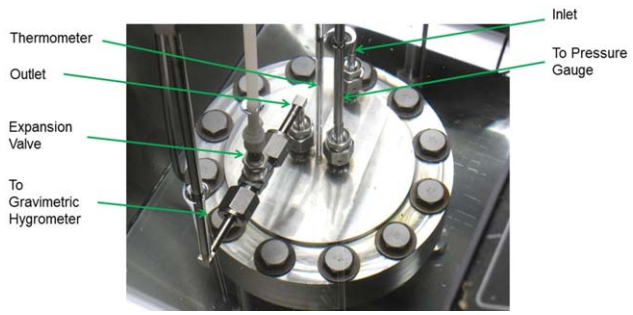

Figure 3. Photograph of the final saturator.

[Color figure can be viewed in the online issue, which is available at wileyonlinelibrary.com.]

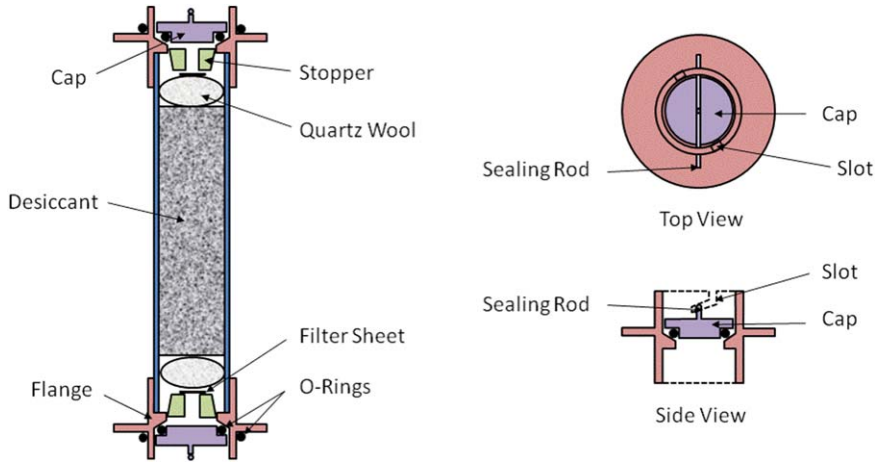

Figure 4. Schematic diagram of the water collection tubes used in the gravimetric hygrometer.

[Color figure can be viewed in the online issue, which is available at wileyonlinelibrary.com.]

For each measurement of y_w, a nominal amount of moist gas is passed through the gravimetric hygrometer. This amount is determined so that approximately 1 g of water will be collected during the passage. As the moist gas passes through the gravimetric hygrometer, the water is trapped in three collection tubes containing the desiccant magnesium perchlorate ($Mg(ClO_4)_2$). The remaining dry gas is directed to a gas collection system.

The design of the water collection tubes is shown in Figure 4. The tubes have caps that allow them to seal the tubes while mounted inside the hygrometer's manifold. The caps are sealed to the tubes by compressing elastomer O-rings using special tools mounted in the manifold. When sealed, the caps ensure that the gas inside the collection tubes will not mix with the ambient air. A second set of elastomer O-rings seals the tubes to the manifold. All O-rings mentioned above are Teflon-encapsulated to prevent absorption/desorption of moisture and gas in the elastomers.

After the tubes are mounted in the hygrometer manifold, the manifold is purged and flushed with fresh dry gas of the same type used during the measurement. This process is repeated three times to ensure all ambient air and moisture are removed from the manifold. The purging is performed with a molecular drag pump to keep the manifold clean.

The masses of all three collection tubes are measured both before and after the gas is passed through them. The masses are measured by comparison against a standard mass using a commercial electronic balance with a range of 200 g and a resolution of 10^{-5} g. The mass measurements are corrected for buoyancy. The mass change of the gas in the tubes is determined and subtracted from the total mass change, yielding the mass change due to water collection (m_w). Only the first two tubes are intended to collect water; the third tube is intended to verify that all water was collected in the first two tubes. In the collection tubes, one batch of desiccant is used for several measurements; once the first tube collects over 10 g of water, the desiccants in the first two tubes are replaced.

The design of the gas collection system is shown in Figure 5. The system consists of two prover pistons. As gas is collected in the prover tubes, the pistons rise. With gas access controlled by computer-controlled pneumatic valves, the two prover pistons alternate in collecting gas, allowing continuous automated collection. A laser interferometer system is used to accurately determine the vertical position of the pistons. As the inner diameters of the prover tubes are known from earlier dimensional measurements, the volume of gas under each piston can be calculated by its vertical position. Once a piston reaches a certain height (58 cm), a valve automatically opens the gas to the other piston. As the second piston rises, pressure and temperature measurements are made underneath the first piston. Afterward, a valve opens to allow the gas collected under the first piston to escape, allowing the piston to fall to its original position. A second measurement of pressure and temperature under the piston is made. Afterward, the first piston is kept in place until its gas-access valve is reopened. The temperature and pressure measurements and the gas's equation of state[14] are used to calculate the density of the gas underneath the piston. The volume and density measurements are then used to calculate the total gas mass increment. At the end of the measurement of y_w, all gas mass increments are summed to provide the total gas mass.

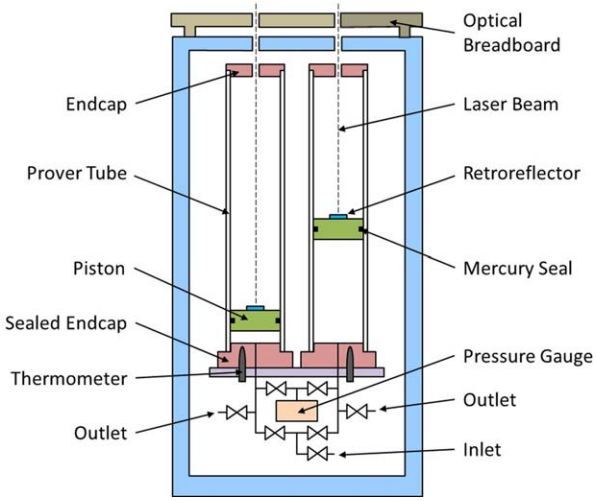

Figure 5. Schematic diagram of the gas collection system used in the gravimetric hygrometer.

[Color figure can be viewed in the online issue, which is available at wileyonlinelibrary.com.]

For the measurements presented in this article, the gravimetric hygrometer was used as described in Ref. 16 with a few exceptions. First, instead of using $Mg(ClO_4)_2$ in the first two water collection tubes and phosphorous pentoxide (P_2O_5) in the third, $Mg(ClO_4)_2$ was used in all three tubes. This change was made after determining that P_2O_5 did not capture any measureable amount of water that was not already captured by the $Mg(ClO_4)_2$. Second, the two sets of O-rings used to seal the water collection tubes were made of Teflon-encapsulated elastomers rather than ordinary elastomers. This change prevented absorption/desorption of moisture and gas in the elastomers, and made a significant improvement on the repeatability of the measurements. Finally, for measurement of water amount fractions corresponding to dew points higher than ambient temperature at ambient pressure, we heated the gravimetric hygrometer manifold section leading to the first water collection tube. Heating tape was wrapped around this section and it was heated to 95 °C to prevent any moisture condensation inside.

When the gravimetric hygrometer manifold was partially heated, special steps were taken to ensure that the pressure in the water collection tubes was at ambient both before and after the moist gas was passed through. After the manifold was heated but before the gas passage, the tube caps were opened and the pressure in the manifold was increased to about 120 kPa for a few seconds using dry gas; the manifold was then briefly vented to the room to reduce the pressure to ambient. After the gas passage and with the tube caps still open, the manifold was cooled to ambient temperature. The pressure in the manifold was then increased to about 120 kPa for a few seconds using dry gas; afterward the manifold was briefly vented to the room to reduce the pressure to ambient.

Measurement uncertainty

The total uncertainty of a quantity v is related to the n individual uncertainty components w_i through the general law of error propagation[19]

$$u(v)^2=\sum_{i=1}^{n}\left(\frac{\partial v}{\partial w_i}\right)u(w_i)^2+2\sum_{i=1}^{n-1}\sum_{j=i+1}^{n}r_{i,j}\frac{\partial v}{\partial w_i}\frac{\partial v}{\partial w_j}u(w_i)\,u\left(w_j\right) \tag{7}$$

The relevant quantities and the derivatives $\partial v/\partial w_i$ may be found by expanding the differential dv

$$\mathrm{d}v=\sum_{i=1}^{n}\frac{\partial v}{\partial w_i}\mathrm{d}w_i \tag{8}$$

The total uncertainty for the water-vapor enhancement factor $f(T_{DP}, p)$ is obtained by applying Eq. 8 to Eq. 5, which yields

$$\mathrm{d}f=\frac{y_w}{e}\mathrm{d}p+\frac{p}{e}\mathrm{d}y_w-\frac{py_w}{e^2}\mathrm{d}e \tag{9}$$

In de, we can separate out the differential relating to the uncertainty of its calculating equation de^{calc} from that relating to the uncertainty of the temperature from which it is calculated

$$\mathrm{d}e=\mathrm{d}e^{calc}+\frac{\mathrm{d}e}{\mathrm{d}T_{DP}}\mathrm{d}T_{DP} \tag{10}$$

Combining Eqs. 9 and 10 and dividing by f gives

$$\frac{\mathrm{d}f}{f}=\frac{\mathrm{d}p}{p}+\frac{\mathrm{d}y_w}{y_w}-\frac{\mathrm{d}e^{calc}}{e}-\frac{1}{e}\frac{\mathrm{d}e}{\mathrm{d}T}dT \tag{11}$$

The relative uncertainty $u_r(f)$ in the water vapor enhancement factor may then be expressed as

$$u_r(f)^2\equiv\frac{u(f)^2}{f^2}=\frac{u(p)^2}{p^2}+\frac{u(y_w)^2}{{y_w}^2}+\frac{u\left(e^{calc}\right)^2}{e^2}+\left(\frac{1}{e}\frac{\mathrm{d}e}{\mathrm{d}T}\right)^2u(T)^2 \tag{12}$$

The second term on the right side of Eq. 11 can be related to the uncertainties in m_w and m_g using Eq. 6 to yield

$$\frac{\mathrm{d}y_w}{y_w}=\left[\frac{m_gM_w}{\left(m_wM_g+m_gM_w\right)}\right]\frac{\mathrm{d}m_w}{m_w}-\left[\frac{m_gM_w}{m_wM_g+m_gM_w}\right]\frac{\mathrm{d}m_g}{m_g} \tag{13}$$

Substituting Eq. 6 into Eq. 13

$$\frac{\mathrm{d}y_w}{y_w}=(1-y_w)\frac{\mathrm{d}m_w}{m_w}-(1-y_w)\frac{\mathrm{d}m_g}{m_g} \tag{14}$$

The second term on the right side of Eq. 12 may then be expressed as

$$\frac{u(y_w)^2}{{y_w}^2}=(1-y_w)^2\frac{u(m_w)^2}{{m_w}^2}+(1-y_w)^2\frac{u(m_g)^2}{{m_g}^2} \tag{15}$$

The relative uncertainty in the water vapor enhancement factor may then be expressed as

$$u_r(f)^2=\frac{u(p)^2}{p^2}+(1-y_w)^2\frac{u(m_w)^2}{{m_w}^2}+(1-y_w)^2\frac{u(m_g)^2}{{m_g}^2}+\frac{u\left(e^{calc}\right)^2}{e^2}+\left(\frac{1}{e}\frac{\mathrm{d}e}{\mathrm{d}T}\right)^2u(T)^2 \tag{16}$$

The relative uncertainty for the water mass, determined by comparison of the water collection tubes against a standard mass using an electronic balance with a sensitivity mass (see "Gravimetric hygrometer" section), is given in Eq. 11 of Ref. 16

$$\frac{u(m_w)^2}{{m_w}^2}=\frac{10{\rho_a}^2[V_t-V_s]^2}{{m_w}^2}\cdot\left[\frac{u(p_a)^2}{{p_a}^2}+\frac{u(T_a)^2}{{T_a}^2}+\left(\frac{1}{\rho_a}\frac{\mathrm{d}\rho_a}{\mathrm{d}(RH)}\right)^2u(RH)^2\right]+\frac{17u\left(m'\right)^2}{{m_w}^2}+\frac{u(m_{sens})^2}{{m_w}^2}+\frac{u(m_{esc})^2}{{m_w}^2} \tag{17}$$

Here, V_t is the volume of the collection tube, V_s is the volume of the mass standard, p_a is the ambient pressure during the mass measurement, T_a is the ambient temperature during the mass measurement, ρ_a is the density of the ambient air, RH is the relative humidity of the ambient air, m' is the measured mass of a collection tube, and m_{sens} is the mass of the sensitivity mass. Finally, m_{esc} is the mass of the water that may have escaped the water collection tubes (assumed to be 0 g).

The uncertainty of the gas mass is given in Eq. 13 of Ref. 16

$$\frac{u\left(m_g\right)^2}{m_g^2}=\frac{u(A)^2}{A^2}+\frac{u(\Delta z)^2}{\Delta z^2}+\frac{u\left(p_g\right)^2}{p_g^2}+\frac{u\left(T_g\right)^2}{T_g^2} \tag{18}$$

Here, A is the cross-sectional area of the prover tubes, p_g and T_g are the pressure and temperature of the gas in the

Table 1. Uncertainty Elements for the Dew-Point Measurement Facility

Description	Symbol	Uncertainty	Contribution to $u_r(f) \times 100$
Saturation System			
Saturator pressure	p	0.0001 p	1.0×10^{-2}
Saturator temperature	T_{DP}	0.005 K	$\leq 3.5 \times 10^{-2}$
Water vapor-pressure calculation	e^{calc}	$4.4 \times 10^{-5}\ e^{calc}$	4.4×10^{-3}
Water Mass Measurement			
Mass measurements	m'	7.0×10^{-5} g	$1.5 \times 10^{-2}(1 - y_w)$
Sensitivity mass	m_{sens}	1.2×10^{-4} g	$6.0 \times 10^{-3}(1 - y_w)$
Air pressure	p_a	25 Pa	$4.0 \times 10^{-3}(1 - y_w)$
Air temperature	T_a	0.2 K	$1.0 \times 10^{-2}(1 - y_w)$
Air relative humidity	RH	1 %	$5.0 \times 10^{-3}(1 - y_w)$
Water escaping collection tubes	m_{esc}	7.5×10^{-8} mg	$7.5 \times 10^{-6}(1 - y_w)/y_w$
Gas Mass Measurement			
Gas temperature	T_g	0.1 K	$3.4 \times 10^{-2}(1 - y_w)$
Gas pressure	p_g	13 Pa	$1.3 \times 10^{-2}(1 - y_w)$
Prover tube piston displacement	Δz	4.7×10^{-3} cm	$7.8 \times 10^{-3}(1 - y_w)$
Prover tube area	A	9.0×10^{-3} cm^2	$5.5 \times 10^{-3}(1 - y_w)$
Relative Combined Expanded Uncertainty ($k = 2$): $U_r(f) \times 100 = 0.12$, where $U_r(f) = U(f)/f$			

prover tubes, respectively. Also, Δz is the piston displacement at which the piston prover stops rising and the gas volume is measured, and its uncertainty is given by

$$u(\Delta z)^2 = u(z_1)^2 + u(z_2)^2 \tag{19}$$

Here, z_1 is the piston position before gas enters the prover tube and z_2 is the piston position after the gas stops entering the tube.

The uncertainty budget for the elements listed above is shown in Table 1. The absolute uncertainty values are shown in the third column of the table, and the contribution of the element to $u_r(f) \times 100$ is shown in the fourth column. As the highest value of y_w measured is ≈ 0.1, most contributions are nearly constant. However, the contribution from T varies from 2.0×10^{-2} to 3.5×10^{-2}. The contribution for m_{esc} is negligible for most values of y_w measured for this article. The largest contribution (for $y_w = 5.8 \times 10^{-4}$) was 1.3×10^{-2} and the smallest (for $y_w = 9.7 \times 10^{-2}$) was 6.9×10^{-5}. The relative combined expanded uncertainty with a coverage factor of $k = 2$, $U_r(f) = 2u_r(f)$, ranged from $U_r(f) \times 100 = 0.10$ to $U_r(f) \times 100 = 0.12$. For simplicity, we estimate $U_r(f)$ to be $U_r(f) \times 100 = 0.12$ for measurements made with this facility. Additional contributions to the uncertainty, specific to the experiments conducted in this work, will be discussed in a subsequent section.

Validation of the facility

As the saturation system of the dew-point measurement facility had never been used before, we first performed measurements of $f(T, p)$ in CO_2-free air to validate the system. These values of f are well known and can be calculated using Eq. 18 of Ref. 5. Therefore, we considered the agreement of our measurements of f with these values to be an appropriate validation of the saturation system.

The measurements were performed with the saturator temperature controlled at 21.67 °C. The gas used was CO_2-free air. The gas supplier specified the air to have CO < 1 μL/L, CO_2 < 0.1 μL/L, H_2O < 0.5 μL/L, NO_x < 50 nL/L, O_2 20–21%, SO_x < 50 nL/L, and total hydrocarbons < 0.05 μL/L. We did not perform a separate analysis of the gas composition. A high-purity regulator was used with the air cylinder.

The pressures used were over the range 0.25 to 6.5 MPa. The results of the comparison are shown in Figure 6. Here, the relative difference, $(\Delta f)_r$, given by

$$(\Delta f)_r = [f(\text{measured}) - f(\text{calculated})]/f(\text{calculated}) \tag{20}$$

is shown as a function of pressure. The agreement of all points is within 0.2, and the standard deviation of all the $\Delta f/f$ values is 0.10%, which is consistent with the uncertainty of the facility.

The measurements shown in Figure 6 were performed with flow rates ranging from 2 to 6 SLM. For example, the three measurements shown at 1 MPa were performed with flow rates of 2.0, 3.4, and 3.8 SLM, and these measurements showed no systematic variation of f with flow rate. The good agreement of all measurements with the calculated values demonstrates that the system saturates fully for flow rates over this range.

Results

We performed measurements of $f(T, p)$ using CO_2 on six isotherms: 10, 21.7, 30, 40, 60, and 80 °C, and 0.5 MPa ≤ p ≤ 5.0 MPa. For most isotherms, the data were taken at 10 pressure values from 0.5 to 5.0 MPa in increments of 0.5 MPa. However, for the 10 °C isotherm, data were not

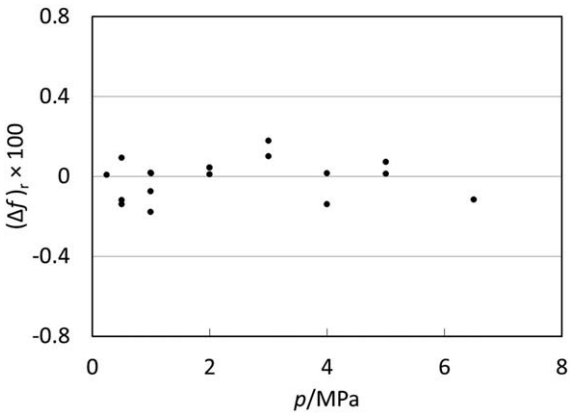

Figure 6. Comparison of measurements of the water-vapor enhancement factor $f(T, p)$ in CO_2-free air with known values calculated using Eq. 18 of Ref. 5.

The measurements were all made at $t = 21.7$ °C. Here, $(\Delta f)_r = [f(\text{measured}) - f(\text{calculated})]/f(\text{calculated})$.

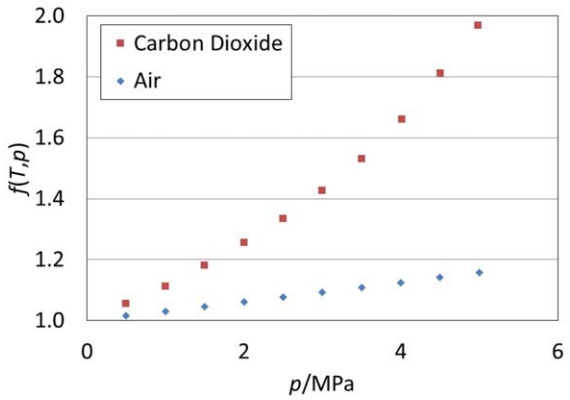

Figure 7. Comparison of measurements of $f(T, p)$ in CO_2 with those in CO_2-free air.

The values of f are plotted as a function of p on the isotherm $t = 21.7$ °C. The air data are those shown in Figure 6. [Color figure can be viewed in the online issue, which is available at wileyonlinelibrary.com.]

taken above 4 MPa because CO_2-H_2O hydrates are known to form in this range.[20]

For most measurements, the manifold connecting the saturation system to the first desiccant tube of the gravimetric hygrometer was not heated, because the generated dew-point temperature at ambient pressure was below the ambient temperature. However, for pressures of 0.5 to 1.5 MPa on the 60 °C isotherm and pressures of 0.5 to 4.0 MPa on the 80 °C isotherm, the dew-point temperature was above ambient temperature. For this case, we heated the tube connecting the final saturator to the inlet of the gravimetric hygrometer to 120 °C and we heated the gravimetric hygrometer tube between the inlet and the first desiccant tube to 95 °C to prevent water condensation in these areas.

Shown in Figure 7 is a comparison of the data for CO_2 and air. Here, $f(T, p)$ is shown as a function of p on the isotherm $t = 21.7$ °C. The air data are those from our validation experiments shown in Figure 6. The values of f for CO_2 are considerably higher than those for air, with values of $(f - 1)$ ranging from 3 to 6 times greater. These higher values show that the attractive interaction between water molecules and CO_2 molecules is considerably stronger than the average interaction between water molecules and the ensemble of molecules present in air.

Values for all the data are listed in Table 2, and these values are plotted in Figure 8. The data are presented for six isotherms: 10, 21.7, 30, 40, 60, and 80 °C. As shown in the figure, the value of f increases nearly proportionally with pressure but with some upward curvature. The curvature is very small at the higher temperatures but becomes more apparent as the temperature is decreased. For a given pressure, the value of f decreases as the temperature increases.

Table 2. Measured Values of the Saturator (Dew-Point) Temperature T, Saturator Pressure p, Saturated Water Amount Fraction y_w, and Water-Vapor Enhancement Factor f, for the Six Isotherms Measured in This Work

T (K)	p (MPa)	$y_w \times 10^3$	f
283.15	0.5002	2.6064	1.0614
283.15	1.0004	1.3886	1.1310
283.15	1.5007	0.9925	1.2127
283.15	2.0028	0.8016	1.3073
283.15	2.4986	0.6944	1.4128
283.15	3.0182	0.6293	1.5466
283.15	3.5009	0.5916	1.6866
283.15	3.9937	0.5812	1.8898
294.83	0.5000	5.4788	1.0557
294.83	1.0003	2.8883	1.1134
294.83	1.5005	2.0413	1.1805
294.83	2.0008	1.6239	1.2523
294.83	2.5010	1.3849	1.3348
294.83	3.0013	1.2332	1.4274
294.84	3.5016	1.1338	1.5299
294.84	4.0112	1.0738	1.6599
294.84	4.5027	1.0445	1.8125
294.84	4.9854	1.0244	1.9681
303.14	0.5002	8.8966	1.0482
303.15	1.0003	4.6867	1.1038
303.14	1.5008	3.2833	1.1608
303.15	2.0008	2.6054	1.2273
303.14	2.5013	2.2033	1.2982
303.15	3.0013	1.9371	1.3689
303.14	3.5017	1.7714	1.4611
303.15	4.0019	1.6650	1.5689
303.14	4.5020	1.5719	1.6672
303.15	5.0055	1.5022	1.7705
313.17	0.5002	15.340	1.0381
313.17	1.0003	8.0707	1.0919
313.17	1.5007	5.6219	1.1410
313.17	2.0010	4.4139	1.1949
313.17	2.5012	3.7211	1.2589
313.17	3.0013	3.2649	1.3252
313.17	3.5016	2.9370	1.3914
313.17	4.0019	2.7320	1.4787
313.16	4.5022	2.5664	1.5635
313.17	5.0024	2.4569	1.6623
333.19	0.5000	41.504	1.0386
333.18	1.0002	21.461	1.0743
333.18	1.5007	14.798	1.1118
333.18	2.0009	11.514	1.1534
333.18	2.5010	9.5623	1.1974
333.18	3.0012	8.2871	1.2451
333.18	3.5015	7.3862	1.2948
333.18	4.0018	6.7515	1.3504
333.17	4.5019	6.2355	1.4059
333.18	5.0024	5.8609	1.4681
353.15	0.4999	97.482	1.0280
353.15	1.0001	50.406	1.0633
353.14	1.5005	34.562	1.0941
353.15	2.0007	26.675	1.1257
353.14	2.5010	21.942	1.1576
353.14	3.0012	18.871	1.1948
353.15	3.5017	16.681	1.2320
353.14	4.0016	15.051	1.2705
353.15	4.5020	13.793	1.3095
353.15	5.0023	12.819	1.3523

Thermodynamic Analysis

Description of phase equilibrium

At vapor-liquid equilibrium in the mixture of CO_2 (component 1) and H_2O (component 2), the fugacity of each component in the liquid phase must equal that in the vapor phase. For water, we can write this rigorously as[21]

$$\gamma_2 x_2 f_2^{\text{pure}}(T,p) = \phi_2 y_2 p \tag{21}$$

where x and y denote mole fractions in the liquid and vapor phases, respectively, γ_2 is an activity coefficient representing the deviation from ideal-solution behavior, $f_2^{\text{pure}}(T,p)$ is the fugacity of pure water at the temperature and pressure of the equilibrium, and ϕ_2 is the fugacity coefficient that describes the deviation from ideal-gas behavior in the vapor phase. As the liquid phase at the moderate pressures of interest here

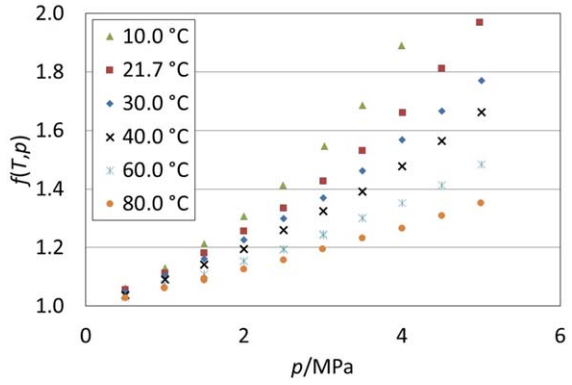

Figure 8. Measurements of $f(T, p)$ in CO_2.

The values of f are plotted as a function of p on the isotherms 10, 21.7, 30, 40, 60, and 80 °C. [Color figure can be viewed in the online issue, which is available at wileyonlinelibrary.com.]

will be nearly pure water, it is reasonable to assume $\gamma_2 = 1$. Also, for convenience we write x_2 as $(1 - x_1)$ for the binary mixture, resulting in our main working equation

$$(1-x_1)f_2^{\text{pure}}(T,p)=\phi_2 y_2 p \tag{22}$$

It is common to compute $f_2^{\text{pure}}(T,p)$ by a multistep process in which the saturation pressure of pure component 2 at temperature T is corrected by a vapor-phase ϕ_2 at saturation of the pure component and a Poynting correction for the effect of pressure on the fugacity. In this case, however, we can compute $f_2^{\text{pure}}(T,p)$ directly from the international standard equation of state for water as implemented in a NIST Standard Reference Database.[15,22]

To a first approximation, the liquid-phase mole fraction of CO_2, x_1, can be computed from Henry's law, where the Henry's constant k_H is defined as the limiting ratio of the fugacity to the liquid-phase mole fraction

$$k_H = \lim_{x_1 \to 0} \frac{f_1}{x_1} \tag{23}$$

where $f_1 = \phi_1 y_1 p$ is the fugacity of component 1. For sparingly soluble gases in water at pressures of a few MPa, it is adequate to remove the limit in Eq. 23 and calculate x_1 directly from the fugacity. However, CO_2 is more soluble in water than most gases, so we add a correction term (known as the Krichevsky-Kasarnovsky equation) for the effect of gas pressure exceeding the vapor pressure of water[21]

$$\ln \frac{f_1}{x_1} = \ln k_H + \frac{\bar{v}_1^{\infty}(p-e(T))}{RT} \tag{24}$$

where $\bar{v}_1^{\infty}$ is the partial molar volume of the solute (CO_2) at infinite dilution in the solvent (H_2O). For $\bar{v}_1^{\infty}$, we use the value 34.2 cm^3/mol that Harvey et al.[23] adopted based on their analysis of the limited data available near ambient conditions. We use values of k_H as a function of temperature from the critical evaluation of Carroll et al.[24] At the highest pressures considered in this work, the Krichevsky-Kasarnovsky correction reduces the solubility x_1 from the Henry's-law value by relative amounts on the order of 5%. Because x_1 is small compared to x_2, this correction corresponds to a tiny but not entirely negligible increase in x_2 and therefore in the equilibrium fugacity of water.

The most important term in Eq. 22 for our thermodynamic analysis is the fugacity coefficient ϕ_2. At the moderate pressures of our experiments, it is sufficient to describe the vapor phase with the virial expansion truncated after the third virial coefficient, as described in the Introduction. The fugacity coefficient for component 2 is then given by[25]

$$\ln \phi_2 = [2(B_{12}y_1 + B_{22}y_2) - B_{\text{mix}}]\left(\frac{p}{RT}\right) + \left[\frac{3}{2}(C_{112}y_1^2 + 2C_{122}y_1y_2 + C_{222}y_2^2) - 2B_{\text{mix}}(B_{12}y_1 + B_{22}y_2) - \left(C_{\text{mix}} - \frac{3}{2}B_{\text{mix}}^2\right)\right]\left(\frac{p}{RT}\right)^2 \tag{25}$$

where B_{mix} and C_{mix} are the mixture second and third virial coefficients given by Eqs. 3 and 4, respectively. With appropriate permutation of subscripts, Eq. 25 is also used to compute ϕ_1 for the fugacity of CO_2 in the solubility calculation of Eq. 24.

Virial coefficients

Equation 25 contains seven virial coefficients: the pure-component values of B and C for each component and the cross coefficients B_{12}, C_{112}, and C_{122}. If these virial coefficients are known, Eqs. 22–25 may be used to calculate values of $f(T,p)$. For pure CO_2, accurate values of B and C may be obtained from the reference-quality equation of state of Span and Wagner.[14] For pure water, values of B from the correlation of Harvey and Lemmon[13] and values of C from the reference equation of state of Wagner and Pruß[15] are used. The values of B_{12}, C_{112}, and C_{122} are not well known. However, using the data from Table 2 along with Eq. 22, it should be possible to determine these values.

When using Eq. 22 to determine virial coefficients from the values of T, p, and f over the range 0–5 MPa, we originally hoped we could assume $C_{112} = C_{122} = 0$ and use the data to determine values of B_{12}. However, when analyzing the data it became clear that this assumption was not valid. We demonstrate this in Figure 9, which shows the relative deviation of the $f(T, p)$ data to the calculated values, $(\Delta f)_r$, where the calculations use values of B_{12} predicted by Wheatley and Harvey[6] and assume $C_{112} = C_{122} = 0$. Although the assumption appears to be valid on isotherms at 30 and 40 °C, the quadratic deviations at other isotherms clearly show that higher-order virial coefficients are needed for accurately calculating $f(T, p)$.

In principle, B_{12}, C_{112}, and C_{122} could all be simultaneously fitted to our experimental data. However, they differ widely in their influence on the phase equilibrium. Because our pressures are not too high, B_{12} is more important than either of the higher-order C coefficients. Also, because y_2 is generally quite small, the contribution of C_{122} is small compared to C_{112}, to the point where the sensitivity of ϕ_2 to C_{122} is almost negligible. We therefore chose to adjust only B_{12} and C_{112} to our data and use estimated values of C_{122}.

We estimated values of C_{122} at our experimental temperatures by the procedure of Hyland and Mason,[26] which takes advantage of the strong water-water interaction to consider the vapor phase as a mixture of (nonpolar) gas molecules, water monomers, and water dimers. The dimerization of water is related to its second virial coefficient B_{22}, and a Lennard-Jones potential is used to describe the interaction of

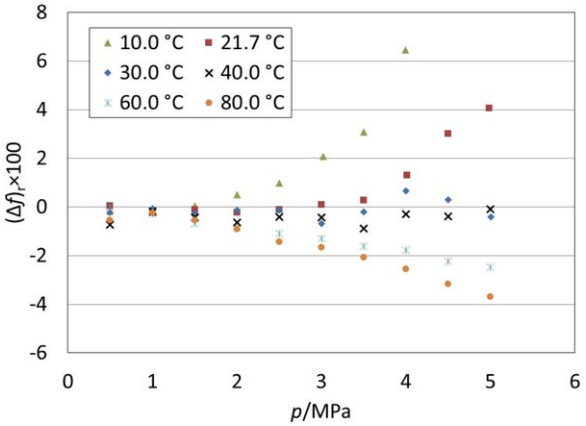

Figure 9. Relative deviations of $f(T, p)$ data to the calculated values, $(\Delta f)_r$, where the calculations use values of B_{12} from Ref. 6 and assume $C_{112} = C_{122} = 0$.

[Color figure can be viewed in the online issue, which is available at wileyonlinelibrary.com.]

the nonpolar gas with the water dimer. Hyland and Mason applied their method to the water-air interaction; we adapted it to our system by using effective Lennard-Jones parameters for CO_2 from Tee et al.[27] and by replacing their older values of B_{22} with those from a current correlation.[13] Hyland and Mason estimate that their technique is only accurate to within a factor of two, but this is adequate for our purposes given the aforementioned insensitivity of the equilibrium to C_{122}. Our estimates for C_{122} are given in Table 3.

With these estimated C_{122}, we first derived initial estimates of B_{12} and C_{112} (and their uncertainties, as described later) based on our experimental values of f on each isotherm, using a simplified version of Eq. 22 that neglected the correction given by Eq. 24 and approximated $f_2^{\text{pure}}(T,p)$ by applying a simple Poynting correction to the vapor pressure. We first varied C_{112} until the deviation $(\Delta f)_r$ was linearly proportional to p. The optimized value of C_{112} was that for which the standard deviation of $(\Delta f)_r$ from a best-fit line, constrained to have a value of $(\Delta f)_r = 0$ at $p = 0$, was minimal. For this determination of C_{112}, we nominally used B_{12} from Wheatley and Harvey,[6] along with our estimated value of C_{122} and the values of B_{11}, B_{22}, C_{111}, and C_{222} from the references mentioned at the beginning of this section. When performing this optimization, the values of $(\Delta f)_r$ above $p = 3.5$ MPa on the 10 and 21.7 °C isotherms were not used, as a good fit was not possible; for the 10 °C isotherm, this may be due to the proximity to the region of CO_2-H_2O hydrate formation; we do not have a clear explanation for the deviation of the high-pressure points on the 21.7 °C isotherm.

Table 4. Optimized Values of the Second Cross Virial Coefficients B_{12}

T (K)	B_{12} (optimized) (cm^3/mol)	$U(B_{12})$ (cm^3/mol)
283.15	−203	3
294.83	−186	2
303.15	−173	6
313.17	−155	5
333.18	−132	2
353.15	−113	3

Our estimate for the expanded uncertainty of the determined B_{12} values is given in the last column.

Once the initial estimate of C_{112} was determined, we estimated B_{12} by minimizing the standard deviation of the ensemble of $(\Delta f)_r$ values. When performing the optimization of B_{12}, the $(\Delta f)_r$ values above $p = 3.5$ MPa on the 10 and 21.7 °C isotherms again were not used. For the determination of B_{12}, we used the estimate of C_{112} described in the previous paragraph and the estimated value of C_{122} along with the values of B_{11}, B_{22}, C_{111}, and C_{222} from the references mentioned earlier.

With these estimates of B_{12} and C_{112} as an initial guess, we then performed a final two-dimensional optimization of their values, using the full model of Eq. 22 described earlier in this section. The optimized values of B_{12} are given in Table 4, and the optimized values of C_{112} are given in Table 3. The values of $(\Delta f)_r$ determined using the optimized values of B_{12} and C_{112} and our estimated values of C_{122} are plotted in Figure 10. All values are within the bounds of the plots except for three of the points not used in the fits: $p = 4.0$ MPa on the 10 °C isotherm [$(\Delta f)_r = 1.97\%$] and $p = 4.5$ and 5.0 MPa on the 21.7 °C isotherm [$(\Delta f)_r = 2.31\%$ and 3.10%, respectively].

Uncertainty Analysis for CO_2-H_2O Measurements

The standard deviation of the points shown in Figure 10 should in principle be within the estimated relative standard uncertainty for the facility described here. This relative uncertainty, calculated above, is $u_r(f) \times 100 = 0.06$. However, the standard deviations of the $(\Delta f)_r$ values plotted in Figure 10, shown in Table 5, are in general larger than this value. We describe here other elements that may contribute to the uncertainty of our measurements with CO_2-H_2O mixtures and provide a final uncertainty estimate.

One uncertainty element particular to CO_2-H_2O mixtures is the effect from the process of carbonation. The unusually high solubility of CO_2 in water results in a process of CO_2 absorption in the water once pressurization begins. Before each measurement was taken, the saturator was at ambient

Table 3. Values of the Third Cross Virial Coefficients C_{122} and C_{112}

T (K)	C_{122} (calculated) (cm^6/mol^2)	C_{112} (optimized) (cm^6/mol^2)	$U(C_{112})$ (cm^6/mol^2)
283.15	−380,000	−14,700	3000
294.83	−290,000	−1800	2000
303.15	−240,000	−500	5000
313.17	−190,000	−3700	6000
333.18	−130,000	1800	1500
353.15	−92,000	5000	3000

The estimated values of C_{122} are calculated using the procedure of Hyland and Mason.[26] The values of C_{112} are optimized as described in the text. Our estimate for the expanded uncertainty of the determined C_{112} values is given in the last column.

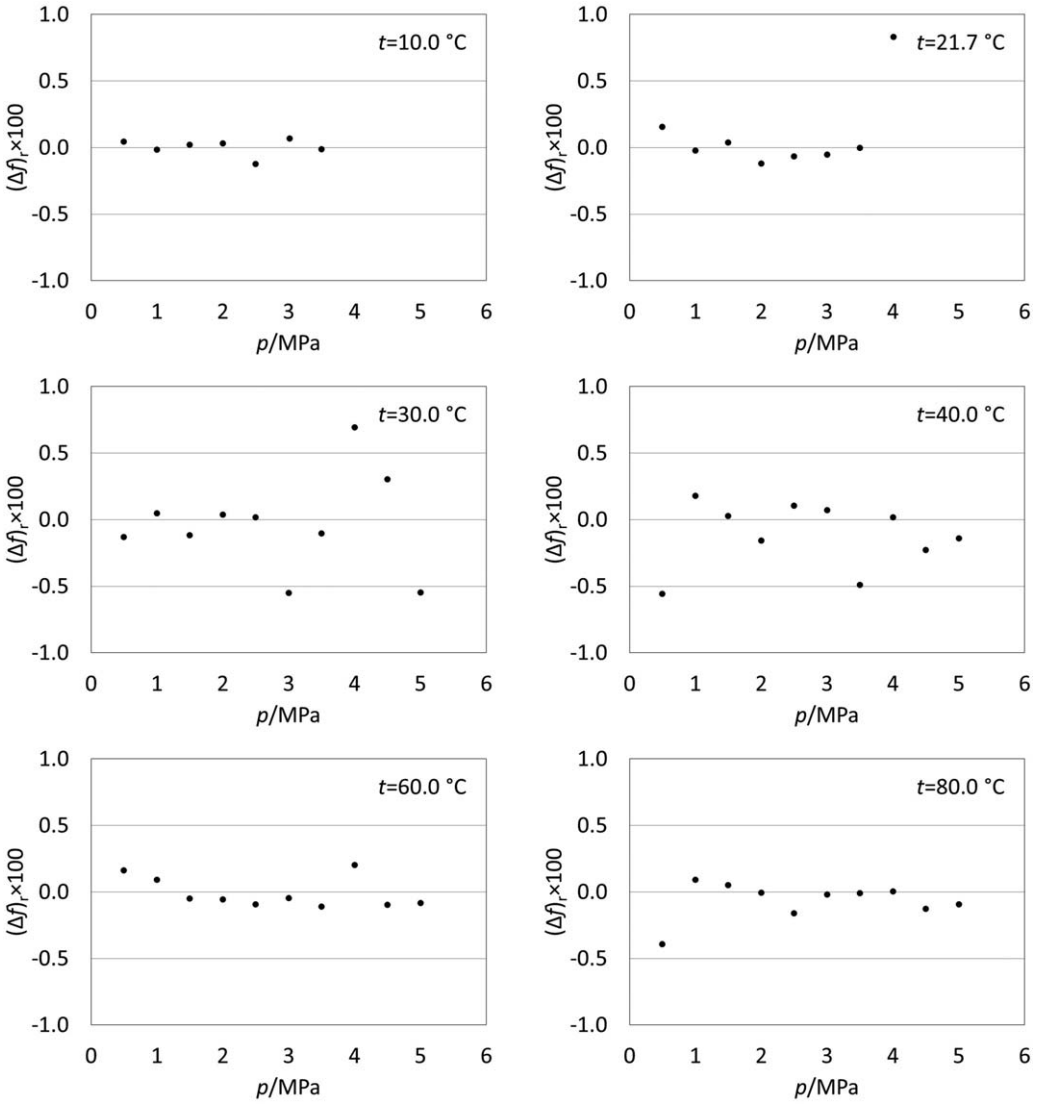

Figure 10. Relative deviations of $f(T, p)$ data to the calculated values, $(\Delta f)_r$, where the calculations use the optimized values of B_{12} and C_{112} given in Tables 4 and 3, respectively, and the calculated C_{122} values given in Table 3.

pressure. Once the saturator was pressurized, our measurements typically began within 20 min. Therefore CO_2 absorption in the water may well have been occurring during our measurements, with the possible effect of the formation of tiny water droplets that may have been carried away by the flowing CO_2, resulting in an excessively large measured value of f.

Another uncertainty element not discussed above is the exchange of air with CO_2 in the water collection tubes of the gravimetric hygrometer when they are briefly cracked open to bring them to ambient pressure. This procedure was done to ensure proper determination of the gas mass inside the tubes. In general, the tube pressure before the cracking was always higher than ambient, so CO_2 leaked out during the cracking. However, if the cracking was not performed carefully, there was always a possibility of a small amount of air leaking in, resulting in an excessively small measured value of f.

Because of these uncertainty elements, whose values are impossible to estimate, we have opted to increase our uncertainty estimates for f by adding them in quadrature with the standard deviation values shown in Table 5. As these values differ for different isotherms, we used individual uncertainties for each isotherm. These uncertainties are given in Table 5 as well. We note that the relative uncertainty in the saturated gas compositions y_w is approximately the same as that for f.

The uncertainty for the virial coefficients may be estimated by examining the sensitivity of the $(\Delta f)_r$ values to changes in B_{12} and C_{112}. The sensitivity of $(\Delta f)_r$ to these

Table 5. Standard Deviation of the $(\Delta f)_r$ Values and Final Relative Combined Expanded Uncertainty $U_r(f)$ of the Water-Vapor Enhancement Factor for Each Isotherm

T (K)	$\sigma[(\Delta f)_r \times 100]$	$U_r(f) \times 100$
283.15	0.06	0.17
294.83	0.07	0.18
303.15	0.37	0.75
313.17	0.25	0.51
333.18	0.08	0.20
353.15	0.15	0.32

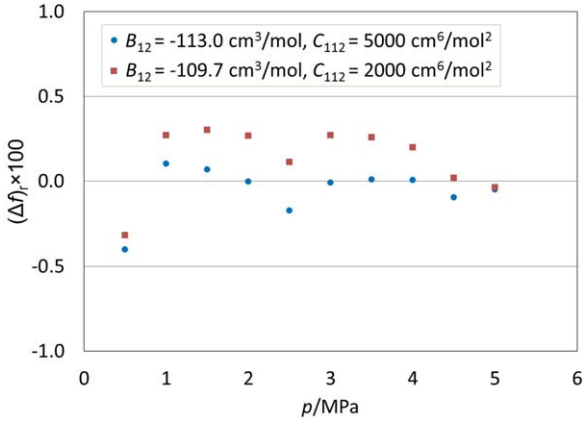

Figure 11. Sensitivity of $(\Delta f)_r$ values to B_{12} and C_{112}.

The plot shows relative deviations of the $f(T, p)$ data to the calculated values, $(\Delta f)_r$, for the isotherm at $t = 80$ °C, where the calculations use values of $B_{12} = -113$ cm³/mol and $C_{112} = 5000$ cm⁶/mol² (the optimized values). Determinations of $(\Delta f)_r$ are also shown for $B_{12} = -109.7$ cm³/mol and $C_{112} = 2000$ cm⁶/mol². The maximum difference between the two sets of $(\Delta f)_r \times 100$ values is 0.3, which is the same as the total relative combined expanded uncertainty $U_r \times 100$ that we have estimated for our determinations of f. [Color figure can be viewed in the online issue, which is available at wileyonlinelibrary.com.]

virial coefficient values is shown in Figure 11. Here, values of $(\Delta f)_r$ are shown for $B_{12} = -113$ cm³/mol and $C_{112} = 5000$ cm⁶/mol² (the optimized values). Values are also shown for $B_{12} = -109.7$ cm³/mol and $C_{112} = 2000$ cm⁶/mol². These latter values were obtained by first adjusting the value of C_{112} by 3000 cm⁶/mol² and afterward adjusting B_{12} so that the $(\Delta f)_r$ values at 5 MPa would agree. We see that the maximum variation in the two sets of $(\Delta f)_r \times 100$ values is approximately 0.3. This is approximately the value that we have estimated for the relative combined expanded uncertainty of our determinations of f at this isotherm. The difference between the two values of B_{12} is 3.3 cm³/mol and that for the two values of C_{112} is 3000 cm⁶/mol². We, therefore, estimate the expanded uncertainty of B_{12} to be $U(B_{12}) = 3$ cm³/mol and that for C_{112} to be $U(C_{112}) = 3000$ cm⁶/mol² on this isotherm. We performed a similar procedure for estimating $U(B_{12})$ and $U(C_{112})$ on the other five isotherms, using the respective values of $U(\Delta f)_r$ for determining the amounts to perturb C_{112} and B_{12}. Our values for $U(C_{112})$ and $U(B_{12})$ are listed in Tables 3 and 4, respectively. It should be noted that C_{112} and B_{12} are correlated (and, therefore, their uncertainties are not independent); a higher C_{112} implies a lower B_{12} and vice versa.

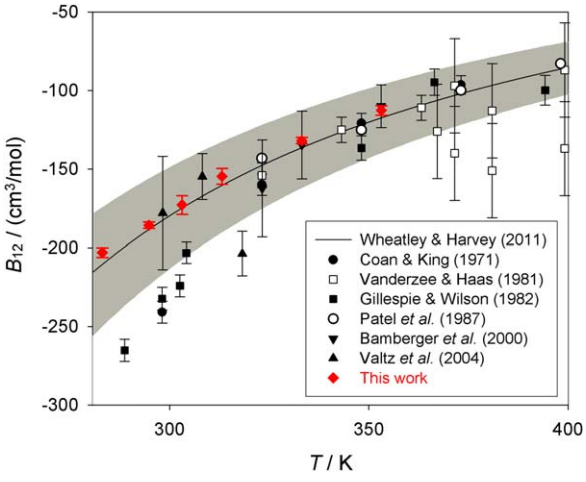

Figure 12. Comparison of the values of B_{12} from this work with those from the predictions of Wheatley and Harvey[6] and from other experiments.[7–10,28,29]

[Color figure can be viewed in the online issue, which is available at wileyonlinelibrary.com.]

In Figure 12, we compare the values of B_{12} determined here to those predicted by Wheatley and Harvey[6] and those from other work.[7–10,28,29] Our results are slightly smaller in magnitude than the predictions of Ref. 6, with the ratio of our values to those of Ref. 6 varying from 0.96 to 0.99. Nevertheless, our values are well within the uncertainties of those of Ref. 6. We also note that the B_{12} values and error bars for other experiments shown in Figure 12 were mostly estimated by Wheatley and Harvey[6] with a method that neglected third virial coefficients; as we have seen in this work (see Figure 9), this assumption would introduce additional error for datasets with data extending above approximately 2 MPa.

Discussion

While not all of the previous experimental studies of the dew point of H_2O in compressed CO_2 reported uncertainties,[7–12] those that did had relative uncertainties of several percent in the water content of the vapor phase. There is no reason to expect that the uncertainties of the other studies were any better. In addition, the existing data are not mutually consistent, as is evident in values of B_{12} derived from the data and shown in Figure 12. In contrast, our experimental uncertainties, as discussed above, are on average 0.3% (relative combined expanded uncertainty with coverage factor $k = 2$, approximately corresponding to a 95% confidence interval). The use of a high-precision gravimetric hygrometer, originally designed for humidity standards, has allowed us to reduce the uncertainty in knowledge of this important quantity by nearly an order of magnitude.

Another result of this work is the validation of the theoretical potential-energy surface and $B_{12}(T)$ of Wheatley and Harvey,[6] as shown in Figure 12. That work had relatively large uncertainties in its derived values of B_{12} at the temperatures studied here; our results (with much smaller uncertainties) lie almost in the center of their uncertainty band. This implies that Wheatley and Harvey might have been overly pessimistic in their uncertainty estimates, or perhaps that they were fortuitous in their theoretical approximations. In any event, the validation of their theoretical results over the temperature range studied in this work means that their B_{12} should also be valid at higher and lower temperatures, enabling those B_{12} to be used as a boundary condition for modeling mixtures (especially gas-phase mixtures) containing H_2O and CO_2 over a wide range of temperatures. There does appear to be a small systematic offset between our results and those of Wheatley and Harvey,[6] so it might be reasonable to reduce the magnitude of their B_{12} values by 2% (in the temperature range studied here) for use in such modeling.

In contrast to B_{12}, the values of C_{112} derived in this work were not determined with high accuracy. We found that small perturbations in the input data, within the scatter of

our measurements, could affect our C_{112} in the second, and sometimes even the first, significant digit. In addition, the optimized values of C_{112} in Table 3 do not vary smoothly with temperature as should be the case. Our results also do not quantitatively line up with an extrapolation of the results of Patel et al.,[29] who reported some C_{112} at higher temperatures. We do not recommend that our C_{112} from Table 3 be used in modeling; they should be viewed as qualitative results that may also be accounting for other experimental effects (such as nonideality in the liquid phase at large CO_2 solubilities) that appear at higher pressures. It might be possible to use modern high-accuracy potential-energy surfaces[6,30] and integration techniques[31] to derive theoretical values of C_{112} that are more reliable than the values we give here, although this would require a physically reasonable model for three-body forces. Recent work by Schultz et al. (submitted) attempts to perform such calculations for C_{112} and C_{122}.

While this work has greatly improved knowledge of the dew points of these mixtures up to 5 MPa, that upper limit is still below pressures that might be encountered in sequestration operations. Such operations might be as high as 20 MPa in the pipeline and 50 MPa in compression for geologic sequestration.[32] These results will still be useful in modeling the high-pressure systems; a physically based model (such as a modern equation of state) that is constrained by good data at moderate pressures will likely be fairly reliable at higher pressures. However, it would be desirable to have some high-pressure data of similar accuracy. Our gravimetric hygrometer could be used for such experiments, but it would require a new high-pressure saturation system, perhaps similar to the high-pressure air saturator designed by Hyland and Wexler.[18]

Acknowledgments

This article is a contribution of the National Institute of Standards and Technology and is not subject to copyright in the United States. This work was supported by the U.S. Department of Energy, National Energy Technology Laboratory, under DOE Interagency Agreement DE-FE0003931. A.H. thanks John Prausnitz for teaching him that even those of us who specialize in theory and modeling should appreciate the value of good experimental work. C.M. thanks John Prausnitz for producing excellent chemical engineers to help understand the results of good experimental work.

Literature Cited

1. Haszeldine RS. Carbon capture and storage: how green can black be? *Science*. 2009;325:1647–1652.
2. Dennis RA, Harp R. Overview of the U.S. Department of Energy's Office of Fossil Energy Advanced Turbine Program for coal based power systems with carbon capture. *Proceedings of ASME Turbo Expo 2007, Vol. 2*. New York: ASME Press, 2007:1093–1104.
3. Figueroa JD, Fout T, Plasynski S, McIlvried H, Srivastava RD. Advances in CO_2 capture technology – the U.S. Department of Energy's Carbon Sequestration Program. *Int J Greenhouse Gas Control*. 2008;2:9–20.
4. Wagner W, Pruss A. International equations for the saturation properties of ordinary water substance. Revised according to the International Temperature Scale of 1990. *J Phys Chem Ref Data*. 1993;22:783–787.
5. Hyland RW, Wexler A. Formulations for the thermodynamic properties of dry air from 173.15 K, and of saturated moist air from 173.15 K to 372.15 K, at pressures to 5 MPa. *ASHRAE Trans*. 1983; 89-IIa:520–535.
6. Wheatley RJ, Harvey AH. Intermolecular potential energy surface and second virial coefficients for the water–CO_2 dimer. *J Chem Phys*. 2011;134:134309.
7. Coan CR, King AD Jr. Solubility of water in compressed carbon dioxide, nitrous oxide, and ethane. Evidence for hydration of carbon dioxide and nitrous oxide in the gas phase. *J Am Chem Soc*. 1971; 93:1857–1862.
8. Gillespie PC, Wilson GM. Vapor-liquid and liquid-liquid equilibria: water-methane, water-carbon dioxide, water-hydrogen sulfide, water-npentane, water-methane-npentane. *GPA Technical Report RR-48*. Tulsa, OK: Gas Processors Association, 1982.
9. Bamberger A, Sieder G, Maurer G. High-pressure (vapor + liquid) equilibrium in binary mixtures of (carbon dioxide + water or acetic acid) at temperatures from 313 to 353 K. *J Supercrit Fluids*. 2000; 17:97–110.
10. Valtz A, Chapoy A, Coquelet C, Paricaud P, Richon D. Vapour-liquid equilibria in the carbon dioxide-water system, measurement and modelling from 278.2 to 318.2 K. *Fluid Phase Equilib*. 2004;226: 333–344.
11. Koglbauer G, Wendland M. Water vapor concentration enhancement in compressed humid nitrogen, argon, and carbon dioxide measured by Fourier transform infrared spectroscopy. *J Chem Eng Data*. 2008; 53:77–82.
12. Hou S-X, Maitland GC, Trusler JPM. Measurement and modeling of the phase behavior of the (carbon dioxide + water) mixture at temperatures from 298.15 K to 448.15 K. *J Supercrit Fluids*. 2013;73: 87–96.
13. Harvey AH, Lemmon EW. Correlation for the second virial coefficient of water. *J Phys Chem Ref Data*. 2004;33:369–376.
14. Span R, Wagner W. A new equation of state for carbon dioxide covering the fluid region from the triple-point temperature to 1100 K at pressures up to 800 MPa. *J Phys Chem Ref Data*. 1996;25:1509–1596.
15. Wagner W, Pruß A. The IAPWS formulation 1995 for the thermodynamic properties of ordinary water substance for general and scientific use. *J Phys Chem Ref Data*. 2002;31:387–534.
16. Meyer CW, Hodges JT, Hyland RW, Scace GE, Valencia-Rodriguez J, Whetstone JR. The second-generation NIST standard hygrometer. *Metrologia*. 2010;47:192–207.
17. Meyer CW, Hodges JT, Huang PH, Miller WW, Ripple DC, Scace GE. *Calibration of Hygrometers with the Hybrid Humidity Generator. NIST Special Publication 250-83*. Gaithersburg, MD: National Institute of Standards and Technology, 2008.
18. Hyland RW, Wexler A. The enhancement of water vapor in carbon dioxide-free air at 30, 40, and 50 °C. *J Res Natl Bur Stand*. 1973; 77A:115–131.
19. ISO. *Guide to the Expression of Uncertainty in Measurement*. Geneva: International Organization for Standardization, 1993.
20. Yang SO, Yang IM, Kim YS, Lee CS. Measurement and prediction of phase equilibria for water + CO_2 in hydrate forming conditions. *Fluid Phase Equilib*. 2000;175:75–89.
21. Prausnitz JM, Lichtenthaler RN, Gomes de Azevedo E. *Molecular Thermodynamics of Fluid-Phase Equilibria, 3rd ed*. Upper Saddle River, NJ: Prentice Hall, 1999.
22. Lemmon EW, Huber ML, McLinden MO. *REFPROP: Reference Fluid Thermodynamic and Transport Properties, NIST Standard Reference Database 23, Version 9.1*. Gaithersburg, MD: National Institute of Standards and Technology, 2013.
23. Harvey AH, Kaplan SG, Burnett JH. Effect of dissolved air on the density and refractive index of water. *Int J Thermophys*. 2005;26: 1495–1514.
24. Carroll JJ, Slupsky JD, Mather AE. The solubility of carbon dioxide in water at low pressure. *J Phys Chem Ref Data*. 1991;20:1201–1209.
25. Yang S, Schultz AJ, Kofke DA, Harvey AH. Interpreting gas-saturation vapor-pressure measurements using virial coefficients derived from molecular models. *J Chem Eng Data*. 2014;59:3183–3192.
26. Hyland RW, Mason EA. Third virial coefficient for air-water vapor mixtures. *J Res Natl Bur Stand A*. 1967;71A:219–224.
27. Tee LS, Gotoh S, Stewart WE. Molecular parameters for normal fluids: the Lennard-Jones 12-6 potential. *Ind Eng Chem Fundam*. 1966; 5:356–363.
28. Vanderzee CE, Haas, NC. Second cross virial coefficients B_{12} for the gas mixture (carbon dioxide + water) from 300 to 1000 K. *J Chem Thermodyn*. 1981;13:203–211.
29. Patel MR, Holste JC, Hall KR, Eubank PT. Thermophysical properties of gaseous carbon dioxide – water mixtures. *Fluid Phase Equilib*. 1987;36:279–299.

30. Hellmann R. *Ab initio* potential energy surface for the carbon dioxide molecule pair and thermophysical properties of dilute carbon dioxide gas. *Chem Phys Lett*. 2014;613:133–138.
31. Singh JK, Kofke DA. Mayer sampling: calculation of cluster integrals using free-energy perturbation methods. *Phys Rev Lett*. 2004; 92:220601.
32. Li H, Jakobsen JP, Wilhelmsen Ø, Yan J. PVTxy properties of CO_2 mixtures relevant for CO_2 capture, transport and storage: Review of available experimental data and theoretical models. *Appl Energy*. 2011;88:3567–3579.

Manuscript received Jan. 29, 2015, and revision received Mar. 25, 2015.